Journal of Applied Physics

Enhanced pulsed thermoacoustic imaging by noncoherent pulse compression

Cite as: J. Appl. Phys. **130**, 174902 (2021); https://doi.org/10.1063/5.0062148
Submitted: 02 July 2021 • Accepted: 12 October 2021 • Published Online: 04 November 2021

Mohand Alzuhiri, Jian Song, Bo Li, et al.

AIP Publishing

Journal of Applied Physics ARTICLE scitation.org/journal/jap

Enhanced pulsed thermoacoustic imaging by noncoherent pulse compression

Cite as: J. Appl. Phys. **130**, 174902 (2021); doi: 10.1063/5.0062148
Submitted: 2 July 2021 · Accepted: 12 October 2021 ·
Published Online: 4 November 2021

Mohand Alzuhiri,[1] Jian Song,[2] Bo Li,[1] Deepak Kumar,[1] Zhen Qiu,[1,3] Jianliang Qian,[2] and Yiming Deng[1,a)]

AFFILIATIONS

[1]Department of Electrical and Computer Engineering, Michigan State University, East Lansing, MI 48823, USA
[2]Department of Mathematics, Michigan State University, East Lansing, Michigan 48823, USA
[3]Institute for Quantitative Health Science and Engineering, Michigan State University, East Lansing, MI 48823, USA and Department of Biomedical Engineering, Michigan State University, East Lansing, Michigan 48823, USA

[a)]**Author to whom correspondence should be addressed:** Dengyimi@egr.msu.edu

ABSTRACT

Microwave-induced thermoacoustic imaging (TAI) is a hybrid imaging technique that combines electromagnetic radiation and ultrasonic waves to achieve high imaging contrast and submillimeter spatial resolution. These characteristics make TAI a good candidate to detect material anomalies that change the material electric properties without a noticeable variation in material density. Conventional pulsed TAI systems work by sending a single short pulse to the imaged target and then detecting the generated pressure signal; therefore, a very high peak power microwave pulse or data averaging is needed to produce images with a high signal-to-noise ratio (SNR). In this paper, we propose to enhance the SNR of pulsed TAI systems by using non-coherent pulse compression. In this approach, a predefined pulse coded signal is used to illuminate the imaged sample and the received pressure signal is cross correlated with a template that is related to the power profile of the excitation signal. The proposed approach can be easily deployed to pulsed TAI systems without the need for major system modifications to the RF source because it only requires a timing circuit to control the triggering time of the RF pulses. In this paper, we demonstrate experimentally that the proposed approach highly improves the SNR of TAI signals and images and can be used to reduce the acquisition time by lowering the number of data averaging or reduce the required peak power from RF sources.

I. INTRODUCTION

Hybrid imaging methodologies combine more than one imaging technique to achieve the best qualities of both. The result of this combination in microwave-induced thermoacoustic imaging (TAI) is a methodology with the high contrast of microwave imaging and fine resolution of ultrasonography.[1] TAI is a hybrid imaging method where an electromagnetic (EM) excitation is used to initiate a fast thermal expansion that generates acoustic waves. The acoustic waves' amplitude is proportional to the local EM absorption and their frequency is related to the pulse width of the excitation EM signal.[2] Therefore, thermoacoustic imaging retains the high contrast of microwave imaging and high resolution of ultrasonography.[3] The thermoacoustic effect was first discovered by Alexander Graham Bell in 1881 when he described the generation of sound waves by an intermittent light source.[4] Thermoacoustic imaging was first proposed by Bowen *et al.*[5] in 1981, and proof-of-concept measurements were subsequently shown in Ref. 6. One of the first publications showing the potential of the imaging methodology was presented by Kruger *et al.* in 1998[7] when they reported successful imaging of a kidney. The sensitivity of TAI imaging to changes in dielectric properties also led to extensive research about adopting TAI for breast cancer imaging where cancerous tissues tend to have higher water content than normal benign tissues.[8–10] Other biomedical applications include but are not limited to prostate cancer detection,[11] blood vessels imaging,[12] and brain tumor imaging.[13] TAI was also proposed for the detection of explosives embedded in a medium with a high water content[1] and the thermoacoustic signals were studied for communications between airborne devices and underwater receivers.[14]

However, the imaging process in TAI systems requires high-power sources to generate acoustic signals with an adequate signal-to-noise ratio (SNR). Typical power sources used in pulsed TAI systems have peak power that ranges from multiple kilowatts[15] to tens of megawatts.[16] On the receiver side, averaging is usually used to reduce the noise power when adopting low peak power sources,[17] but it leads to an increase in the acquisition time; moreover, it is difficult to use averaging when imaging moving objects. Longer RF pulses can also be used to increase the signal-to-noise ratio at the cost of decreasing the spatial resolution of the imaging system.[18] Therefore, several studies were devoted to designing RF sources with high peak power and very short pulses to have a system with high SNR and high spatial resolution.[16,19]

Another approach to improve the SNR is to improve the RF coupling and concentrate the RF power in a small area. Near field RF excitation is used widely in TAI systems to improve the power coupling of the electromagnetic energy to the imaged target.[20,21] Antenna arrays were also suggested to concentrate the electromagnetic power in a small area inside the imaged target.[22] Another approach is to use coded excitation to improve the signal SNR by using a correlation receiver. The use of frequency modulated continuous excitation sources with matched filters on the receiver side highly improves the SNR of TAI systems and allows the usage of low peak power sources.[23] The drawback of this approach is that it requires linear high-power amplifiers; therefore, it is not compatible with the pulsed TAI systems.

In this paper, we propose the use of non-coherent pulse compression (NPC) to improve the SNR of pulsed TAI systems. In this approach, a coded pulse is used to excite the imaged sample and then the received pressure signal is correlated with a template that is related to the power profile of the excitation pulse. The proposed approach does not require the use of linear amplifiers; therefore, it can be easily applied to pulsed TAI systems without major modification. The approach only requires control over the timing of the pulse excitation. The proposed method highly enhances the received signal SNR when compared with the pulsed TAI system with the same peak power and number of averages. A pulsed TAI system was built to test the performance of the proposed approach. The results show that the proposed approach can be used to reduce the acquisition time and reduce the microwave source peak power while still having adequate SNR. While we are mainly focusing on pulsed TAI systems in this paper, the proposed approach can also be adapted for photoacoustic imaging (PAI) systems since the two systems share similar principles but differ in the type of contrast mechanism.[24] NPC has already been proposed for applications where pulsed laser diodes are used like in the case of laser range finders[25] and laser radars.[26] The main application for such an approach is to improve the SNR in PAI systems where low-power pulsed laser diodes are being adopted to produce lightweight and low-cost imaging systems.[27–29]

The rest of the paper is organized as follows: Sec. II gives a brief description of the governing equation of TAI signal generations and describes the methods used to apply the noncoherent pulse compression procedure, Sec. III explains the approach used to reconstruct the TAI images, Sec. IV describes the experimental system used to validate the proposed approach, Sec. V discusses the experimental results from the imaging phantoms under different excitation scenarios, and Sec. VI concludes the paper.

II. THEORY OF NPC ENHANCED TAI

A. Fundamentals of thermoacoustic imaging

Thermoacoustic wave generation is an electromechanical phenomenon that results from thermoelastic expansion of a medium due to electromagnetic illumination. The thermal expansion results in a series of mechanical (acoustic) waves that are governed by the wave equation,

$$\Delta^2 p(\vec{r},t) - \frac{1}{c^2(\vec{r})}\frac{\partial^2}{\partial t^2}p(\vec{r},t) = -\frac{\beta(\vec{r})}{k(\vec{r})c^2(\vec{r})}\frac{\partial^2 T(\vec{r},t)}{\partial t^2}, \tag{1}$$

where $c(\vec{r})$, $\beta(\vec{r})$, and $k(\vec{r})$ are the sound speed, volume expansion coefficient, and isothermal compressibility of the medium, respectively. To obtain this model, we have assumed that the medium density varies slowly in space. $p(\vec{r},t)$ is the instantaneous pressure at position $\vec{r}$ and time t. $T(\vec{r},t)$ is the instantaneous temperature of the imaged object at time t and position $\vec{r}$. The left hand side of the equation represents the acoustic wave equation, while the right hand side of the equation represents the thermoacoustic source. The instantaneous thermoacoustic source depends on the second derivative of temperature in time while the volume expansion coefficient and the heat capacity are constants that depend on the medium properties. When thermal confinement condition is met, the source part is equal to

$$\rho(\vec{r})\ C_V(\vec{r})\frac{\partial T(\vec{r},t)}{\partial t} = H(\vec{r},t), \tag{2}$$

where $\rho(\vec{r})$ and $C_V(\vec{r})$ are the material density and specific heat capacity of the medium, respectively, and $H(\vec{r},t)$ is a heating function that represents the amount of dissipated energy per unit volume and unit time induced by the excitation pulse. By combining these relations, the thermoacoustic equation is rewritten as

$$\nabla^2 p(\vec{r},t) - \frac{1}{c^2(\vec{r})}\frac{\partial^2}{\partial t^2}p(\vec{r},t) = -\frac{\beta(\vec{r})}{C_p(\vec{r})}\frac{\partial H(\vec{r},t)}{\partial t}, \tag{3}$$

where $C_p(\vec{r}) = \rho(\vec{r})c^2(\vec{r})k(\vec{r})C_V(\vec{r})$ is the specific heat capacity of the medium under constant pressure. The heating function can be written as a product of two separate terms,

$$H(\vec{r},t) = A(\vec{r})I(t), \tag{4}$$

where $A(\vec{r})$ is the absorbed energy per unit volume and time, and $I(t)$ is the temporal envelope of the power of the excitation pulse. Magnetic losses are negligible in nonmagnetic materials; therefore, the total loss is approximated by the sum of conductivity and dielectric loss,

$$A(\vec{r}) = \sigma(\vec{r})|\boldsymbol{E}(\vec{r})|^2 + \omega\varepsilon''(\vec{r})|\boldsymbol{E}(\vec{r})|^2, \tag{5}$$

where $\sigma(\vec{r})$ is the material electrical conductivity, $\varepsilon''(\vec{r})$ is the imaginary part of the permittivity, and $\boldsymbol{E}(\vec{r})$ is the root mean square value of the applied electric field inside the target. The two terms in Eq. (5) describe the conductivity losses and dielectric losses, respectively, and they dominate the thermal energy generation in the tissue.

Under the stress confinement condition, we can express the initial pressure p_0 generated at position $\vec{r}$ as[2,23]

$$p_0(\vec{r}) = \frac{\beta c^2 J(\vec{r})}{C_p}, \tag{6}$$

$$J(\vec{r}) = \int_0^{\tau} H(\vec{r}, t)dt, \tag{7}$$

where $J(\vec{r})$ is the total energy absorbed per unit volume at position $\vec{r}$ during microwave excitation with pulse width τ. This expression indicates that in order to increase the pressure, we can either increase the peak microwave power or increase the pulse width τ.

To obtain the solution for Eq. (1), we can use Green's function for the wave equation. The time dependent Green's function satisfies

$$\left(\nabla^2 - \frac{1}{c^2(\vec{r})}\frac{\partial^2}{\partial t^2}\right) G(\vec{r}, t; \vec{r}', t') = -\delta(\vec{r} - \vec{r}')\delta(t - t'). \tag{8}$$

Then, the pressure wave $p(\vec{r}, t)$ can be obtained by

$$p(\vec{r}, t) = \int\int G(\vec{r}, t; \vec{r}', t')\frac{\beta}{C_p}\frac{\partial H(\vec{r}', t')}{\partial t'} d\vec{r}' dt'. \tag{9}$$

If c is constant and $\vec{r} \in \mathscr{R}^3$, Green's function is given by

$$G(\vec{r}, t; \vec{r}', t') = \frac{1}{4\pi c|\vec{r} - \vec{r}'|}\delta(|\vec{r} - \vec{r}'| - c|t - t'|). \tag{10}$$

Therefore, the formula for the pressure wave can be obtained as

$$p(\vec{r}, t) = \int \frac{1}{4\pi c|\vec{r} - \vec{r}'|}\frac{\beta}{C_p}\frac{\partial H(\vec{r}', t')}{\partial t'}\Big|_{t'=t-|\vec{r}-\vec{r}'|/c} d\vec{r}'. \tag{11}$$

B. Noncoherent pulse compression technique

For signal reconstruction at the receiver end, pulsed TAI systems use averaging to improve the SNR when using low peak power at the microwave source end. Adding two signals increases the signal power by a factor of two while the noise power increases by a factor of $\sqrt{2}$; therefore, the overall SNR increases by a factor of $\sqrt{2}$. With pulse compression, when sending a waveform with twice the energy of the original signal, the signal energy increases by a factor of two while the noise power remains constant; consequently, this leads to an increase in SNR by a factor of 2. Therefore, better overall system efficiency is achieved with a faster acquisition speed.

Pulse compression is a widely used concept in radar systems where the pulse energy is spread over a long time span to avoid the need for high peak power sources, and pulse encoding is used to retain fine range resolution.[30] The simplest example of pulse compression is to increase the pulse length of the excitation signal and lower its amplitude. The drawback of such an approach is that the system resolution will be reduced due to the increase in the width of the excitation pulse. Correlation of such pulse results in a triangular function with a scaling factor that equals to the length of the rectangular excitation pulse. Therefore, pulse coding is used to improve the correlation properties of the received signal. The goal is to create a pulse sequence with a sharp peak at the location of maximum correlation and minimum sidelobes elsewhere. One of the popular sequences are Barker codes due to their low correlation sidelobes, which are inversely proportional to the length of the coding sequence [peak-to-sidelobe ratio (PSL) $= N$ for a sequence with a length of N]. A Barker13 sequence is the longest known sequence of Barker codes and it is given by

$$S_B = [+1\ +1\ +1\ +1\ +1\ -1\ -1\ +1\ +1\ -1\ +1\ -1\ +1]. \tag{12}$$

A single pulse that is coded with Barker13 is shown in Fig. 1(a). With matched filtering, the received signal is correlated with the same profile of the excitation signal. The result of correlating this signal with a matched filter is shown in Fig. 1(b). The correlation result shows a PSL of 13 (equals to the length of the coding sequence), which is expected for this bipolar sequence.

For a pulsed TAI system, unipolar codes are needed because the pulsed radio frequency (RF) source can only alternate between two states of 0 and 1. The EM losses and the generated pressure also only depend on the temporal power profile of the excitation pulse. Using the unipolar sequence of Barker13 that is shown in Fig. 1(c) leads to a degradation in the correlation performance and lowers its peak to sidelobe ratio as shown in Fig. 1(d). The figure shows that the PSL ratio has decreased from 13 to 1.8, which can cause distortion to the detected signal especially in the case of neighboring defects. This low peak to sidelobe ratio is directly related to the unipolar nature of the excitation signal. Two methods can be used to address this degradation effect: mismatched filters and complementary Manchester coded sequences.[31]

1. Mismatched filter

In this approach, the unipolar version of the excitation code is sent without any changes. On the receiver side, the signal is correlated with a weighted function that is designed to minimize the amplitude of sidelobes while maintaining a large peak at zero.

In our experimental setup, we opted to use the maximum peak to sidelobe (MPSL) codes as a pulse coding sequence because they offer longer sequences than Barker codes (Barker codes have a maximum length of 13). An MPSL25 sequence is given by

$$S_{MPSL25} = [1001001010100000011100111]. \tag{13}$$

A more practical version of this code can be achieved by using zero stuffing to ensure constant pulse width across the sequence. This approach ensures that the resolution is governed by the pulse width that is used in the sequence. A zero stuffed MPSL25 is given by

$$S_{MPSL25z} = [1000001000001000100010000 \\ 0000000001010100000101010]. \tag{14}$$

A graphical representation of the zero stuffed MPSL25 is shown in Fig. 2(a). A mismatched filter with a length of 150 (three times the

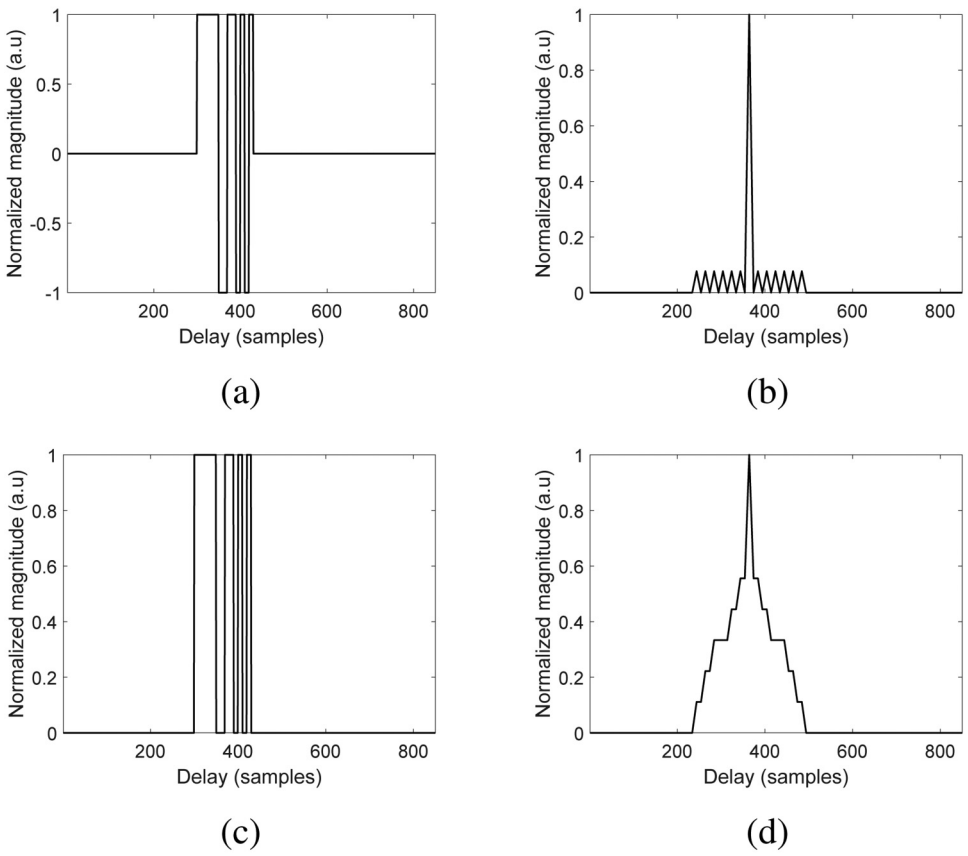

FIG. 1. (a) A single pulse coded with bipolar Barker13 sequence, (b) the results of correlating a signal coded with bipolar Barker13 with a its matched filter, (c) a single pulse coded with unipolar Barker13 sequence, and (d) the results of correlating a signal coded with a unipolar Barker13 with its matched filter.

length of the excitation sequence) is shown in Fig. 2(b). A cross correlation of the MPSL25 code with the mismatched filter template is shown in Fig. 2(c). The results show highly suppressed sidelobes when compared to matched filtering results (PSL = 56.4).

2. Complementary Manchester coded pairs

Complementary pairs have unique correlation characteristics where the summation of the autocorrelation functions results in zero sidelobes.[32] This property is associated with using a bipolar signal of −1 and 1; therefore, using a unipolar sequence degrades the correlation performance. One solution to this problem is to use Manchester coding to convert the code to a unipolar sequence, where every zero is converted to 01 and every one is converted to 10.[33] A unipolar version of a complementary sequence pair with a length of 26 is given by

$$S_{C1} = [00011000101101010110010000], \tag{15}$$

$$S_{C2} = [00001001101000001011100111]. \tag{16}$$

The Manchester coded sequences are given by

$$S_{C1M} = [01010110100101011001101001100110011001101001011001010101], \tag{17}$$

$$S_{C2M} = [01010101100101101001100101010101100110100101101010100101101010]. \tag{18}$$

Graphical representations of S_{C1M} and S_{C2M} are shown in Figs. 3(a) and 3(b), respectively. On the receiver side, each received signal is correlated with its bipolar version (S_{AMB}, S_{BMB}), and the final correlation (R) is then calculated by summing the two correlations together,

$$S_{AMB} = 2S_{AM} - 1,\ S_{BMB} = 2S_{AM} - 1, \tag{19}$$

$$R = \rho_P(S_{AM}, S_{AMB}) + \rho_P(S_{BM}, S_{BMB}). \tag{20}$$

ρ_P refers to the Pearson correlation between two signals. A graphical representation of the summation of the correlation function is shown in Fig. 3(c). The figure indicates high suppression of the sidelobes (PSL = 52). The figure also shows the creation of two negative large peaks in the vicinity of the main peak of correlation that can lead to a distortion in the final reconstructed TAI image.

III. IMAGE RECONSTRUCTION

Various approaches have been proposed for image reconstruction from thermoacoustic signals.[34–38] The performance of these algorithms varies depending on the sound speed property and

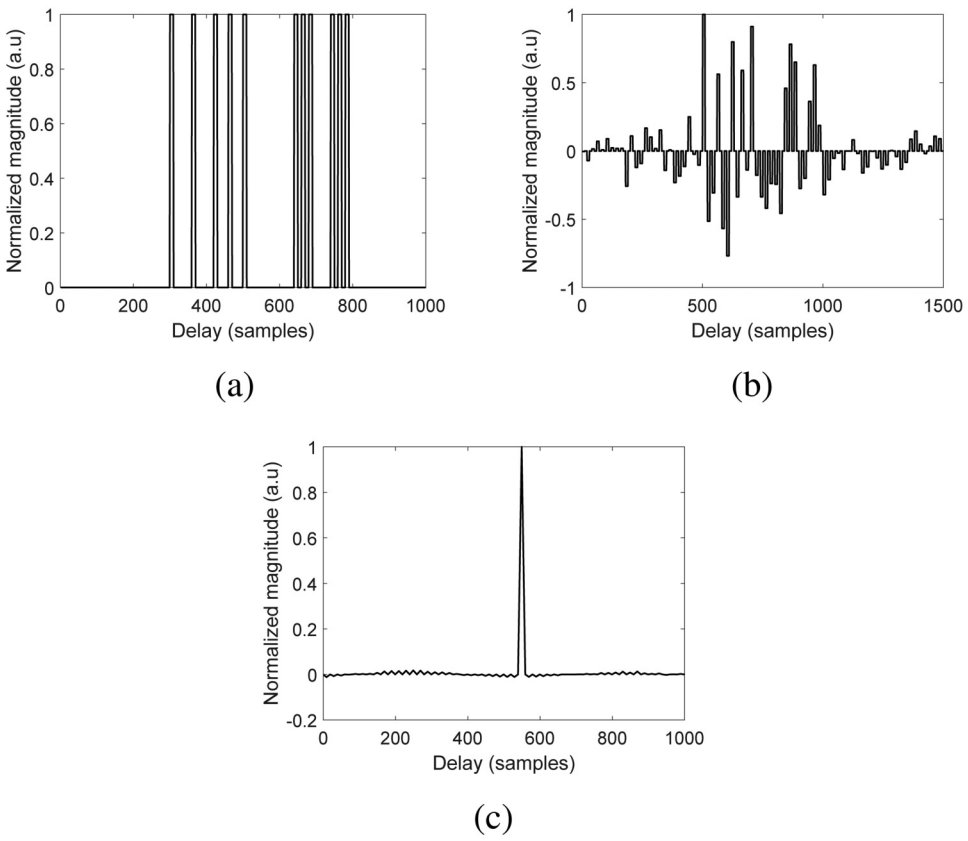

FIG. 2. (a) Zero stuffed MPSL25 sequence, (b) mismatched filter for zero stuffed MPSL25, and (c) correlation results of MPSL25 with the mismatched filter.

observation surface geometry.[39] The time-reversal method has been shown to be the least restrictive. Due to the simplicity and robustness, the time-reversal-based method is used to reconstruct the image in the implementation.

Time reversal is based on the reciprocity of the wave equation which means that we can re-transmit the measured signal on a closed surface in a time-reversed chronology to uniquely reconstruct its source. According to Huygens' principle, if the sound speed is constant and the spatial dimension is odd, the wave leaves a bounded domain in a finite time for any initial source with a bounded support; in other words, there is a time $\mathscr{T}$ when the pressure wave fields become zero inside the observation domain for any $t > \mathscr{T}$; therefore, we can set the pressure wave to be zero at time $\mathscr{T}$, and we then use the measured data on the observation surface to uniquely reconstruct the initial source in the reversed time series; in this case, the initial source can be reconstructed exactly. When the sound speed is not constant or the spatial dimension is even, the pressure wave does not vanish at any time in the observation domain; the local decaying results given in Ref. 39 indicate that, in this case, the time-reversal method can also give a good approximation. To improve the TAI mage quality, an advanced method based on the Neumann–Series approach is further developed.[40,41]

To obtain optimal reconstruction, the time-reversal method requires full-aperture information. However, this is not applicable in practice. In the experiment, we only have a limited number of transducers distributed on the observation surface. In order to have better reconstruction from limited data, we need to interpolate the measurement data onto a continuous measurement surface and then reconstruct the image using the time-reversal method.[42–45] This technique has been widely used to improve the quality of reconstructed image. Here, a simulation with a limited number of transducers evenly distributed on the measurement surface is performed to reemphasize the necessity of doing the interpolation, and further, we will see this through the experiments. The reconstruction process is implemented by using the Matlab k-Wave toolbox.[42] Figure 4 shows the reconstruction results of the two methods. Figure 4(a) shows the simulated geometry with the positions of transducers indicated. Figures 4(b) and 4(c) show the reconstructions from the time-reversal method without and with interpolation of the measurement data, respectively. Figure 4(d) shows a comparison of the reconstructions along the line shown in Fig. 4(a). The results show that the edges of the original image are blurred when reconstructing the image without interpolation of the data. Reconstruction with the interpolation of the data can sharpen the edges and improve the contrast significantly as shown in the figures, since the data set is enriched by interpolating the measurement data onto the measurement surface.

IV. MEASUREMENT SETUP

A thermoacoustic imaging system in its simplest form mainly consists of an RF excitation source and an ultrasound sensor that

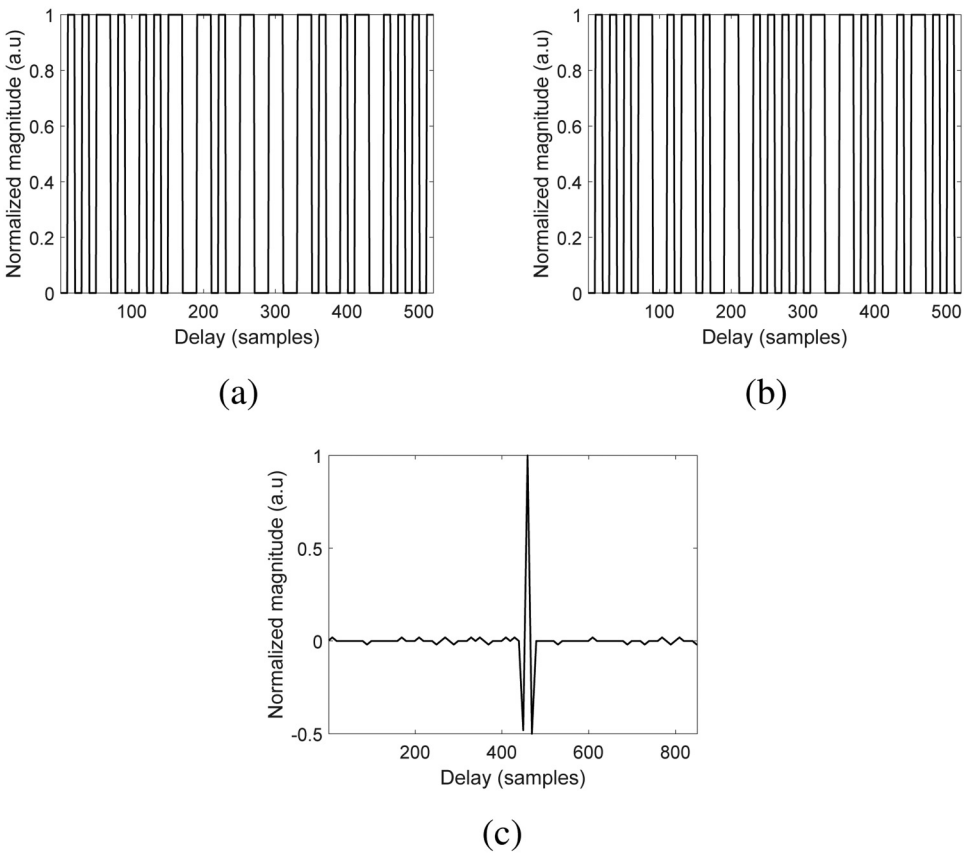

FIG. 3. (a) First waveform of the Manchester coded complementary sequence, (b) second waveform of the Manchester coded complementary sequence, and (c) summation of the correlation function.

collects the generated ultrasound waves. In the experiment, we built a computed tomography system to produce 2D sectional images of the imaged samples. The thermoacoustic wave was excited by an Epsco PG5KB pulsed microwave source with 5 kW maximum excitation and an operating frequency of 2.45 GHz. The pulse width can be varied from 0.3 to 30 μs. An open-ended waveguide was used to couple the RF signal to the imaged target. An open-ended waveguide was used due to the high-power density in the near field when compared to a horn antenna.[46] The waveguide is connected to a glass tank that is filled with mineral oil. Mineral oil acts as a coupling medium for the ultrasound waves from the imaged target to the ultrasonic transducer. Mineral oil also has low dielectric constant and low electromagnetic losses in the frequency range of the excitation signal. These factors are necessary for reducing the reflections from the excitation antenna (open-ended waveguide) and increasing the contrast of the imaged object when compared to the imaging medium. The ultrasound signals were collected by using an Olympus V306 transducer with a center frequency of 2.25 MHz to capture the high frequency components from the 0.5 μs excitation pulses.

The ultrasound transducer was connected to an Olympus pulse receiver with a low noise amplifier with 60dB of gain. The amplifier is connected to a DSOX4052A oscilloscope as a data acquisition device. The oscilloscope also has a pulse generator that is responsible for providing the excitation waveform for the RF source and the required clock for the data acquisition process. During the scanning process, the imaged sample is attached to a rotating arm that is controlled by a stepper motor and placed on the top of the open-ended waveguide. During the acquisition process, a pulsing trigger is sent to start the RF excitation and the ultrasound acquisition process simultaneously. After finishing each acquisition process, the motor is rotated to collect data from multiple angles around the imaged sample and provide 360^{circ} coverage. A diagram illustrating the system's main components is shown in Fig. 5(a) and a picture of the experimental setup is shown in Fig. 5(b).

To validate the experimental setup, we created a test sample with known internal defects. The sample consists of a rectangular cheese body with two agar inclusions as shown in Fig. 6(a). This sample was chosen because it has a small amount of material density variations while the significant contrast is provided by the difference in EM losses. A CT image of the sample is shown in Fig. 6(b), and it shows a homogeneous material density across the imaged sample. For the TAI image, the test sample was excited with 0.5 μs microwave pulse with 4.5 kW peak power, and the averaging was set to 1024 on the acquisition side. The data were collected at 50 angles around the imaged target by rotating the target in front

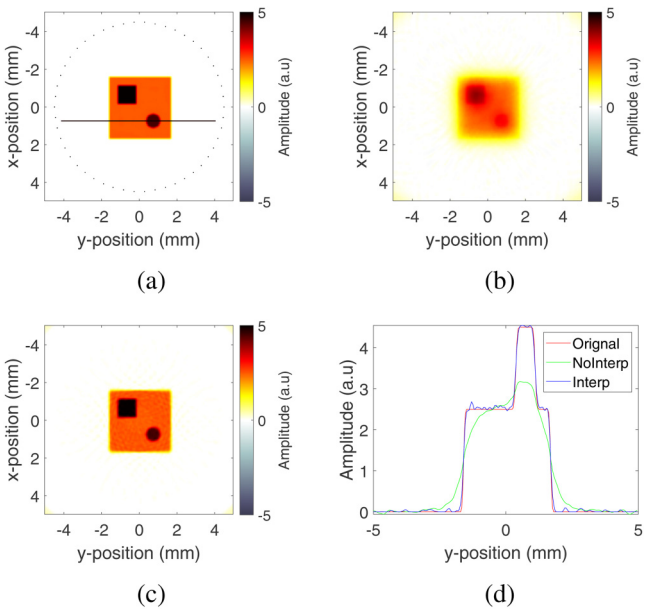

FIG. 4. Effect of interpolation of the measurement data: (a) the simulated geometry with 50 transducers evenly distributed on a circle, (b) the reconstruction without interpolation of the measurement data, (c) the reconstruction with the interpolation of the measurement data, and (d) the detailed comparison at the line shown in (a).

of the ultrasound transducer at a rate of 7.2^{circ}/rotation. The data were then fed to a time-reversal algorithm to reconstruct the structure of the imaged target.[42] The reconstructed TAI image without interpolation of measurement data is shown in Fig. 6(c). Figure 6(d) shows the reconstruction with the interpolation of measurement data. Since the agar inclusions have higher water content than the cheese, they experience a higher amount of EM losses and generate stronger TAI signals. As a result, the TAI image shows higher pixel values for the regions where the agar inclusions are located due to the higher amount of EM absorption as mentioned earlier.

V. RESULTS AND DISCUSSION

A. NPC on 1D signal

To test the performance of the proposed approaches, a cheese sample with a single agar core was used to create a test sample with known signal characteristics. A picture of the imaged sample is shown in Fig. 7(a). The black arrow indicates the direction of the data collection. In the beginning, the sample is imaged with a single pulse approach to have a reference of the shape of the expected TAI signal. The source power was set to 3 kW and the averaging on the oscilloscope was set to 2048 to reduce the noise in the acquired signal. A 1D signal acquired from the side of the sample is shown in Fig. 7(b). Region 1 represents the RF coupling to the ultrasound (US) transducer. Region 2 represents the effect of the RF pumping on the US amplifier. Region 3 indicates the front wall of the sample. Region 4 represents the agar inclusion. Region 5 represents the signal from the second wall of the sample. Finally, region 6 represents the pressure signal from the reflections inside the imaged sample. We notice that there are no continuous intensity values in the received signal due to the effect of the limited bandwidth of transducers, and such a band-limited transducer acts as a bandpass filter to the received signal.

The experiment was repeated with the MPSL25 and complementary code sequences. The raw signal acquired with the MPSL25 excitation is shown in Fig. 8(a). The resulting signal after applying the mismatched filter is shown in Fig. 8(b). The figure shows that the signal retains the same features that exist in the original signal with a lower amount of noise. The raw signals acquired with the Manchester coded complementary sequences are shown in Figs. 9(a) and 9(b), respectively. The summation of the signals after applying the matched filtering is shown in Fig. 9(c). The figure shows that the main regions of the signal can be identified but with a large amount of distortion.

To test the performance against noise, we reduced the averaging from 2048 to 2. The direct acquisition results show that it is difficult to identify any of the main regions in the single pulse signal as shown in Fig. 7(c). The mismatched filtering output shows the improved SNR performance (11dB), and the regions can be clearly identified as shown in Fig. 8(c). With the complementary Manchester coding, we can see a slight improvement over the

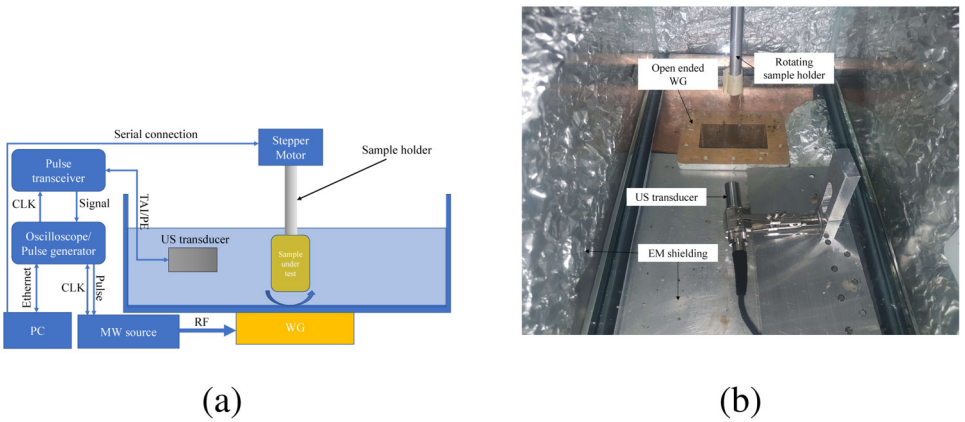

FIG. 5. (a) Schematic of the experimental setup and (b) photographic picture of the experimental setup.

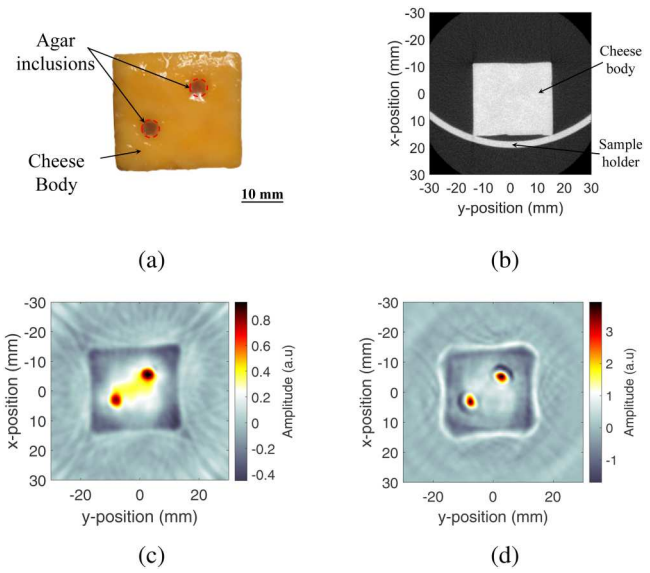

FIG. 6. Experimental system validation: (a) picture of the scanned sample, (b) cross-sectional CT image of the scanned sample, (c) reconstructed TAI image without interpolation, and (d) reconstructed TAI image with interpolation.

single pulse approach, but the performance is lower than that of the matched filters approach as shown in Fig. 9(d).

B. NPC on 2D images

In this section, we are showing the effect of using the proposed approach on the reconstructed images. The experimental system in Sec. IV is used to acquire 2D images of test samples under different configurations. Manchester coded complementary pairs approach requires a longer time than the direct transmission approach because it requires the use of two excitation signals. This approach also requires a slightly more complex source because it requires the RF source to transmit pulses with different pulse widths. On the other hand, the mismatched filter approach uses fixed pulse width; therefore, it only requires control of the pulse start time. The Manchester coded complementary pairs approach also has a larger amount of distortion; therefore, we only used the mismatched filter approach for the 2D comparison.

The test sample is the same sample that was used for the 1D comparison in Sec. V A and is shown in Fig. 7(a). Similar to the 1D comparison, the sample is imaged with a single pulse approach to have a reference of the shape of the expected TAI image. The images were collected with 3 kW peak power and 256 averages. The 2D TAI image of the imaged sample with a single pulse excitation

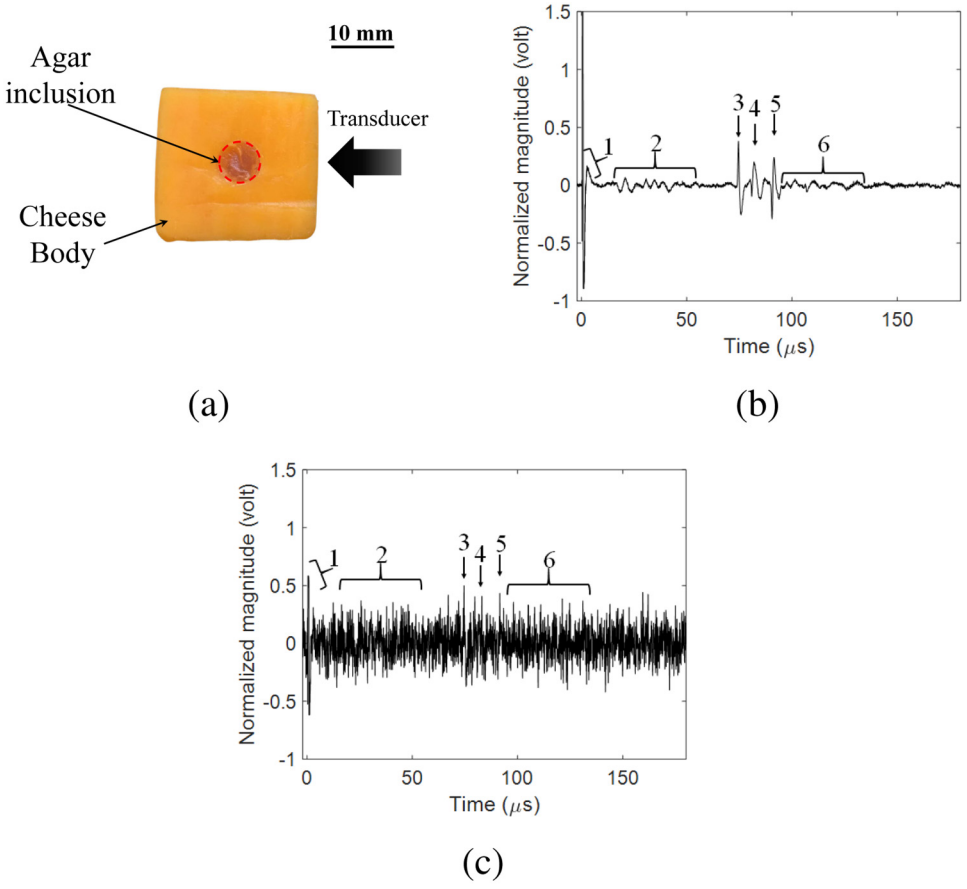

FIG. 7. 1D TAI signal with single pulse excitation: (a) cheese sample with agar core, (b) 1D signal acquired at 3 kW excitation and 2048 averages, and (c) 1D signal acquired at 3 kW excitation and 2 averages.

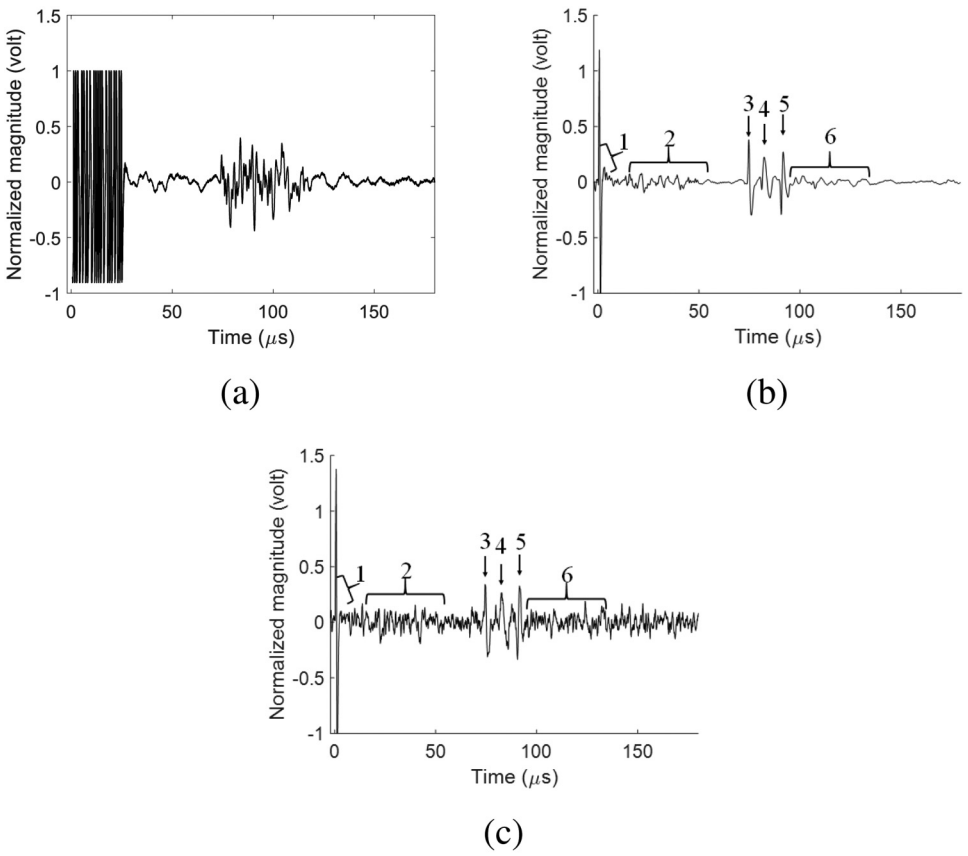

FIG. 8. 1D TAI signal with MPSL25 excitation and a mismatched filter: (a) raw signal acquired with 2048 averages, (b) filtered signal with 2048 averages, and (c) filtered signal with 2 averages.

is shown in Fig. 10(a). The image acquired with the MPSL25 coded excitation is shown in Fig. 10(b). A 1D comparison of the reconstructed images along a horizontal line that passes through the center of the agar core is shown in Fig. 10(c). The imaging results show a successful reconstruction of the edges of the imaged sample, and the agar core can be identified in the middle of the reconstructed frames. Peak signal-to-noise ratio (PSNR) is used to provide a quantitative measure of the reconstruction image quality when comparing two images. Given two images I and I' with dimensions of $m \times n$, the PSNR is calculated as follows:

$$\mathrm{PSNR} = 10\log_{10}\left(\frac{M^2}{MSE}\right), \tag{21}$$

$$MSE = \frac{1}{mn}\sum_{i=0}^{m-1}\sum_{j=0}^{n-1}[I(i,j) - I'(i,j)]^2, \tag{22}$$

where M is the maximum possible value of the pixel in the image, I is the reference image, and I' is the noisy image. The reference image was created by repeating the imaging with a single pulse and 2048 averages to ensure low noise levels as shown in Fig. 10(d). Table I shows the experiment parameters and a comparison of the PSNR from the single and MPSL25 excitation. The results show that the MPSL25 image has a higher PSNR value than the single pulse image with an improvement of 10.555 dB which agrees with the observations from the direct comparison of the images.

1. Reduction of the acquisition time

The proposed approach can be used to increase the acquisition speed by reducing the system dependence on signal averaging. To demonstrate this feature, an experiment was performed with the same aforementioned system configuration but the averaging was reduced from 256 to 2. The 2D reconstruction results with the single pulse excitation are shown in Fig. 11(a). The results show that it is difficult to identify the boundaries of the imaged sample and we can only identify the agar core in the middle of the image. The 2D reconstruction results for the MPSL25 excitation are shown in Fig. 11(b). The reconstruction results show that the image still retains all the information about the imaged object. A 1D comparison of the reconstructed images along a horizontal line that passes through the center of the agar core is shown in Fig. 11(c). Table II shows the experiment parameters and a comparison of the PSNR from the single and MPSL25 excitation. The results show that the

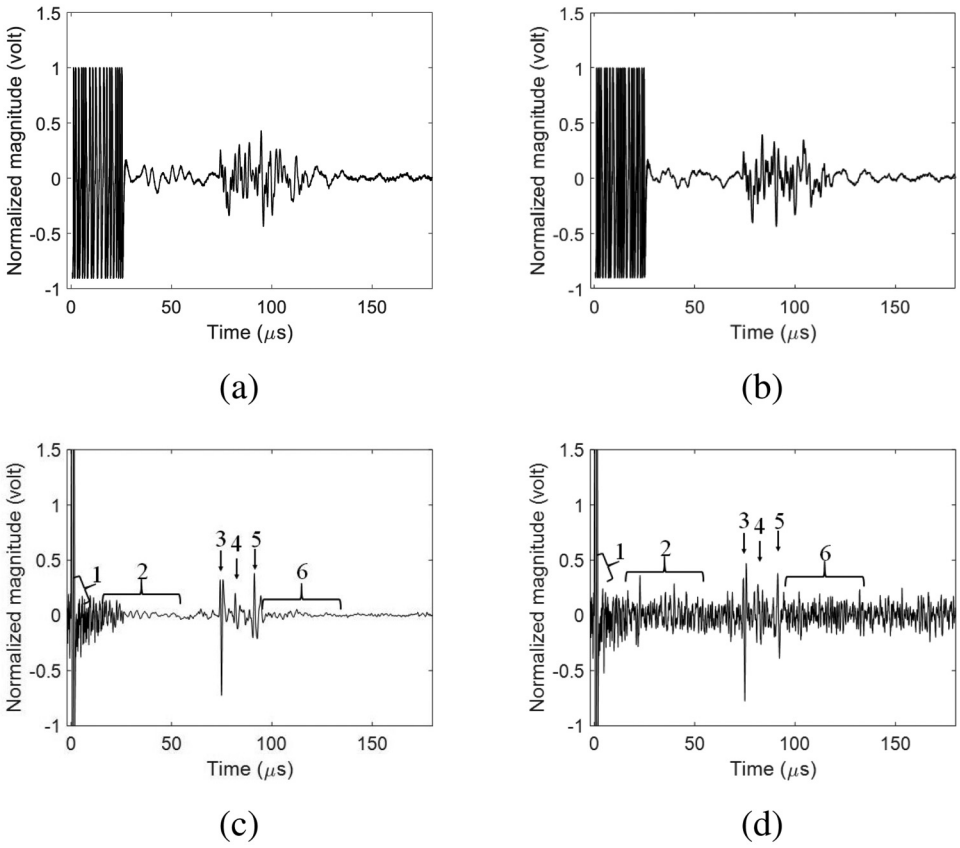

FIG. 9. 1D TAI signal with Manchester coded complementary pairs excitation: (a) first raw signal with 2048 averages, (b) second raw signal with 2048 averages, (c) summation of the correlation function with 2048 averages, and (d) summation of the correlation function with 2 averages.

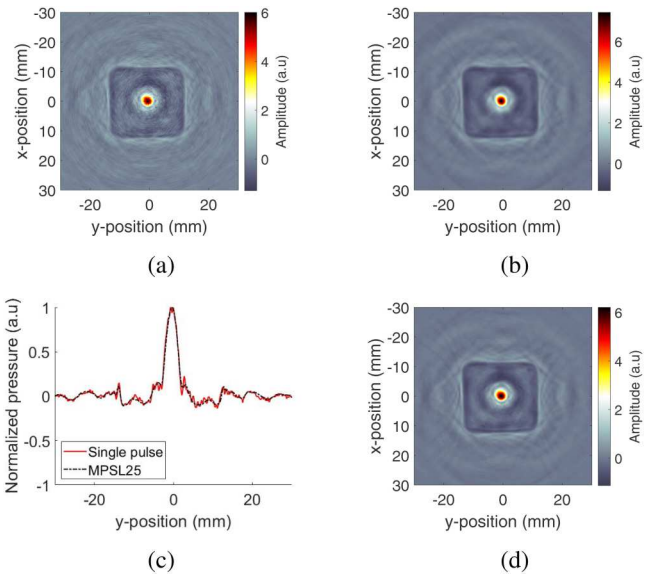

FIG. 10. 2D TAI images of the inspected object: (a) reconstruction with single pulse excitation, (b) reconstruction with MPSL25 excitation, (c) 1D comparison of the reconstructed images along a horizontal line that passes through the center of the agar core, and (d) reference image.

image with MPSL25 excitation continues to have a higher PSNR value than the single pulse excitation with a difference of 16.88 dB.

2. Reduction of the system peak power

With constant excitation pulse width and fixed acquisition speed, we can reduce the system peak power to enable the usage of low peak power RF sources. To demonstrate this feature, the system power was reduced from 3 to 1.5 kW and the averaging was kept at 256. The 2D reconstruction results for the single pulse and MPSL25 excitation are shown in Figs. 12(a) and 12(b), respectively. A 1D comparison of the reconstructed images along a horizontal line that passes through the center of the defect is shown in Fig. 12(c) and the quantitative comparison is shown in Table III. The results show that the image reconstruction with MPSL25 excitation continues to have a better performance than the single pulse excitation and the PSNR value is improved by 11.32 dB.

TABLE I. Quantitative comparison of reconstruction with single and MPSL25 excitation.

Method	averages	Power (kW)	PSNR (dB)
Single	256	3	31.58
MPSL25	256	3	42.1350

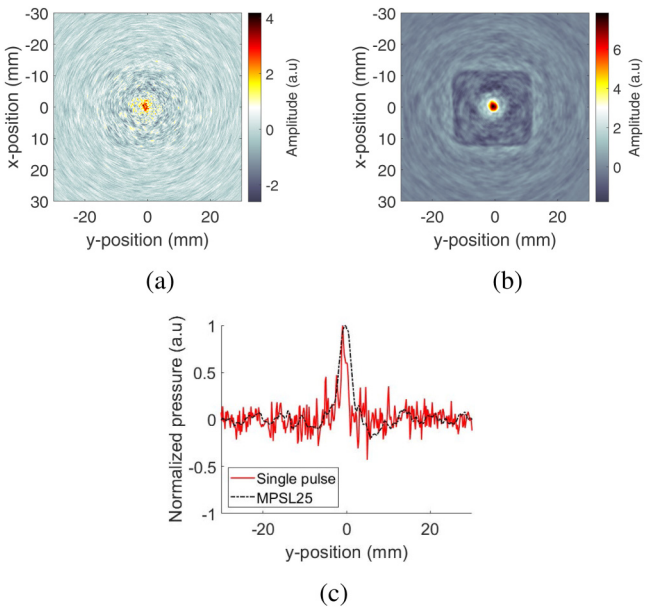

FIG. 11. Comparison of reconstruction with reduced acquisition time with 0.5 μs at 3 kW and 2 averages: (a) single pulse, (b) MPSL25, and (c) 1D comparison of the reconstructed image at the center of the defect.

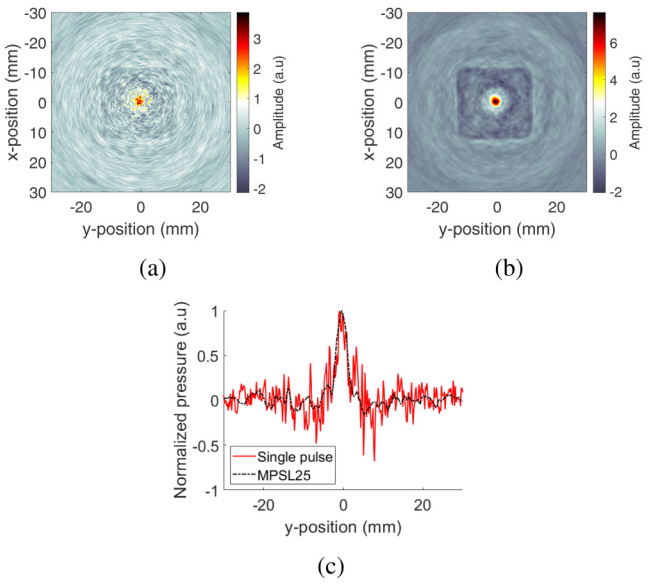

FIG. 12. Comparison of reconstruction with reduced peak power excitation with 0.5 μs pulse width at 1.5 kW: (a) single pulse, (b) MPSL25, and (c) 1D comparison of the reconstructed image at the center of the defect.

3. Increasing the system spatial resolution while maintaining high SNR

Spatial resolution in TAI systems is highly dependent on the pulse width of the excitation signal. The generated TAI signal represents an integration of a sphere with a volume that is proportional to the width of the excitation pulse. Therefore, reducing the pulse width increases the system spatial resolution but at the same time reduces the amount of energy injected into the system which results in a reduced SNR. Here, we demonstrate that with the coded excitation, we can increase the imaging spatial resolution without sacrificing the system SNR in low-power pulsed TAI systems.

To validate that experimentally, a new sample with a cylindrical agar body and two metallic inclusions was created. Figure 13(a) shows a schematic of the structure of the imaged target. The agar sample has a diameter of 27.3 mm and the inclusions are metal wires with a diameter of 0.6 mm. In the beginning, the sample was imaged with high peak power excitation of 3 kW and 0.5 μs to serve as a reference for the low-power results and the imaging results can be seen in Fig. 13(b). In this image, we can identify both of the wire inclusions and we can identify the boundary of the agar sample. The power was then reduced to 2 kW to simulate a low-power RF system. We started the demonstration by performing imaging with a 2-μs pulse and the imaging results are shown in Fig. 14(a). We notice that we can only identify a single wire in the image but with an enlarged footprint when compared to the reconstruction in Fig. 13(b). We then reduced the pulse width to 1 μs and the imaging results can be seen in Fig. 14(b). Reducing the pulse width improves the system's spatial resolution and both of the wires can be identified but with an increased amount of noise. Further reducing the pulse width to 0.5 μs as shown in Fig. 14(c) leads to a deterioration in the image SNR where it is difficult to identify the edges of the agar sample due to the large amount of noise. Finally, the coded excitation with MPSL25 was used with 0.5-μs pulse width and the results are shown in Fig. 14(d). The results show that the proposed approach can improve the system's spatial resolution while maintaining adequate SNR. A 1D comparison along a line that passes through the two inclusions is shown in Fig. 14(e). The figure includes a comparison between the image in Fig. 13(b) as a reference (Ref.) and the reconstruction results in Figs. 14(b)–14(d).

TABLE II. Quantitative comparison of reconstruction with reduced acquisition time.

Method	averages	Power (kW)	PSNR (dB)
Single	2	3	12.5797
MPSL25	2	3	29.4600

TABLE III. Quantitative comparison of reconstruction with reduced excitation power.

Method	averages	Power (kW)	PSNR (dB)
Single	256	1.5	13.7996
MPSL25	256	1.5	25.1262

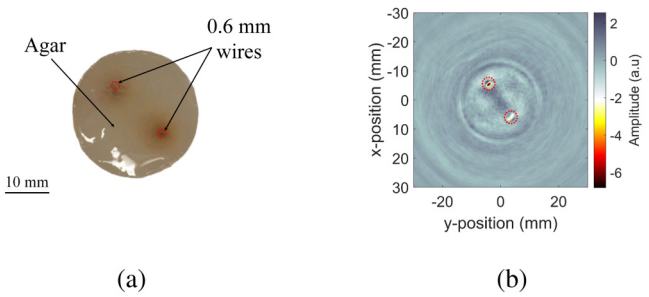

FIG. 13. (a) Structure for the agar sample and (b) TAI image with 0.5 μs single pulse and 3 kW excitation.

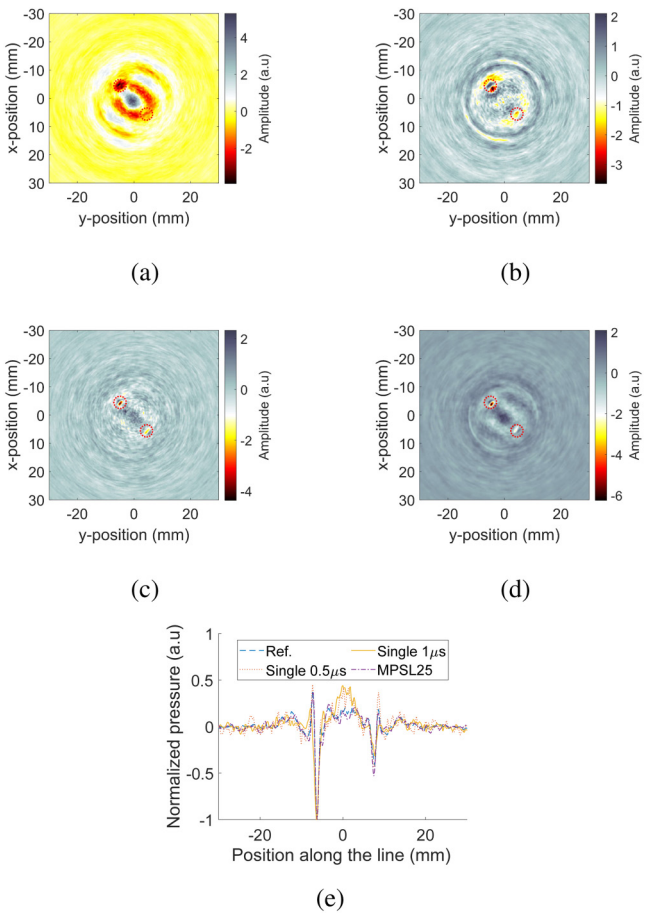

FIG. 14. Comparison of reconstruction with different pulse widths: (a) 2 μs single pulse with 2 kW excitation, (b) 1 μs single pulse with 2 kW excitation, (c) 0.5 μs single pulse with 2 kW excitation, (d) 0.5 μs MPSL-25 coded pulses with 2 kW excitation, and (e) 1D comparison of the reconstructed images along a line that passes through both of the wires.

VI. CONCLUSION

In this paper, we proposed to use noncoherent pulse compression to improve the signal-to-noise ratio in pulsed TAI systems. The proposed approach can be applied to the current pulsed TAI systems without the need for linear radio frequency amplifiers or major system modifications. Experimental results showed that the proposed method highly enhances the received signal SNR when compared with a pulsed TAI system with the same peak power and number of averages. Mismatched filters and complementary Manchester coded sequences were evaluated in this paper, and the results showed that mismatched filters provided better performance, shorter acquisition time, and less complex RF source requirements than complementary Manchester coded sequences. 1D experimental results with mismatched filters showed that the system SNR was improved by 11 dB when using a code sequence with a length of 25 elements. The received signal maintained having similar features to the original signal but with a higher SNR. To validate the imaging capability with the proposed approach, we built a cylindrical imaging system. 2D experimental results showed that the proposed approach can be used to reduce the acquisition time of the TAI signal, employ a microwave source with low peak power, or improve the spatial resolution of low peak power systems while maintaining an adequate level of SNR.

ACKNOWLEDGMENTS

The authors would like to acknowledge Mr. Brian Wright of the MSU ECE shop for his assistance in the fabrication of the experimental system. Qian's research is partially supported by the National Science Foundation (NSF) (Grant Nos. 1614566 and 2012046).

AUTHOR DECLARATIONS

Conflict of Interest

The authors have no conflicts to disclose.

DATA AVAILABILITY

The data that support the findings of this study are available from the corresponding author upon reasonable request.

REFERENCES

[1]X. Wang, T. Qin, Y. Qin, A. H. Abdelrahman, R. S. Witte, and H. Xin, "Microwave-induced thermoacoustic imaging for embedded explosives detection in high-water content medium," IEEE Trans. Antennas Propag. **67**, 4803 (2019).
[2]D. R. Bauer, X. Wang, J. Vollin, H. Xin, and R. S. Witte, "Spectroscopic thermoacoustic imaging of water and fat composition," Appl. Phys. Lett. **101**, 033705 (2012).
[3]Y. Deng and M. Golkowski, "Innovative biomagnetic imaging sensors for breast cancer: A model-based study," J. Appl. Phys. **111**, 07B323 (2012).
[4]A. G. Bell, "On the production and reproduction of sound by light," Am. J. Sci. **s3–20**(118), 305 (1880).
[5]T. Bowen, "Radiation-induced thermoacoustic soft tissue imaging," in *1981 Ultrasonics Symposium* (IEEE, 1981), pp. 817–822.
[6]T. Bowen, R. L. Nasoni, A. E. Pifer, and G. H. Sembroski, "Some experimental results on the thermoacoustic imaging of tissue equivalent phantom materials," in *1981 Ultrasonics Symposium* (IEEE, 1981), pp. 823–827.

[7]R. A. Kruger, K. K. Kopecky, A. M. Aisen, D. R. Reinecke, G. A. Kruger, and W. L. Kiser, "Thermoacoustic CT with radio waves: A medical imaging paradigm," Radiology **211**, 275 (1999).
[8]R. A. Kruger, K. D. Miller, H. E. Reynolds, W. L. Kiser, Jr., D. R. Reinecke, and G. A. Kruger, "Breast cancer *in vivo*: Contrast enhancement with thermoacoustic CT at 434 mHz—Feasibility study," Radiology **216**, 279–283 (2000).
[9]M. Xu, G. Ku, X. Jin, L. V. Wang, B. D. Fornage, and K. K. Hunt, "Breast cancer imaging by microwave-induced thermoacoustic tomography," in *Photons Plus Ultrasound: Imaging and Sensing 2005: The Sixth Conference on Biomedical Thermoacoustics, Optoacoustics, and Acousto-optics* (SPIE, 2005), pp. 45–48.
[10]A. Mashal, J. H. Booske, and S. C. Hagness, "Toward contrast-enhanced microwave-induced thermoacoustic imaging of breast cancer: An experimental study of the effects of microbubbles on simple thermoacoustic targets," Phys. Med. Biol. **54**, 641 (2009).
[11]S. Patch, S. Griep, K. Jacobsohn, W. See, and D. Hull, "Thermoacoustic imaging of prostate cancer: Comparison to histology," in *Photons Plus Ultrasound: Imaging and Sensing 2014* (International Society for Optics and Photonics, 2014), Vol. 8943, p. 894305.
[12]Z. Zheng, L. Huang, and H. Jiang, "Label-free thermoacoustic imaging of human blood vessels *in vivo*," Appl. Phys. Lett. **113**, 253702 (2018).
[13]Y. Xu and L. V. Wang, "Rhesus monkey brain imaging through intact skull with thermoacoustic tomography," IEEE Trans. Ultrason. Ferroelectr. Freq. Control **53**, 542–548 (2006).
[14]X. Wang, T. Qin, Y. Qin, R. S. Witte, and H. Xin, "Microwave-induced thermoacoustic communications," IEEE Trans. Microw. Theory Tech. **65**, 3369 (2017).
[15]G. Ku and L. V. Wang, "Scanning thermoacoustic tomography in biological tissue," Med. Phys. **27**, 1195–1202 (2000).
[16]C. Lou, S. Yang, Z. Ji, Q. Chen, and D. Xing, "Ultrashort microwave-induced thermoacoustic imaging: A breakthrough in excitation efficiency and spatial resolution," Phys. Rev. Lett. **109**, 218101 (2012).
[17]M. Xu, G. Ku, and L. V. Wang, "Microwave-induced thermoacoustic tomography using multi-sector scanning," Med. Phys. **28**, 1958–1963 (2001).
[18]C. Lou, L. Nie, and D. Xu, "Effect of excitation pulse width on thermoacoustic signal characteristics and the corresponding algorithm for optimization of imaging resolution," J. Appl. Phys. **110**, 083101 (2011).
[19]D. Razansky, S. Kellnberger, and V. Ntziachristos, "Near-field radiofrequency thermoacoustic tomography with impulse excitation," Med. Phys. **37**, 4602 (2010).
[20]M. S. Aliroteh and A. Arbabian, "Microwave-induced thermoacoustic imaging of subcutaneous vasculature with near-field RF excitation," IEEE Trans. Microw. Theory Tech. **66**, 577–588 (2017).
[21]S. Kellnberger, A. Hajiaboli, D. Razansky, and V. Ntziachristos, "Near-field thermoacoustic tomography of small animals," Phys. Med. Biol. **56**, 3433 (2011).
[22]H. Nan, S. Liu, J. G. Buckmaster, and A. Arbabian, "Beamforming microwave-induced thermoacoustic imaging for screening applications," IEEE Trans. Microw. Theory Tech. **67**, 464–474 (2018).
[23]H. Nan and A. Arbabian, "Peak-power-limited frequency-domain microwave-induced thermoacoustic imaging for handheld diagnostic and screening tools," IEEE Trans. Microw. Theory Tech. **65**, 2607 (2017).
[24]M. Pramanik and L. V. Wang, "Thermoacoustic and photoacoustic sensing of temperature," J. Biomed. Opt. **14**, 054024 (2009).
[25]D. Kravitz, D. Grodensky, N. Levanon, and A. Zadok, "High-resolution low-sidelobe laser ranging based on incoherent pulse compression," IEEE Photonics Technol. Lett. **24**, 2119–2121 (2012).
[26]M. J. Lindenfeld, "Mismatched filters for incoherent pulse compression in laser radar," IEEE Trans. Aerosp. Electron. Syst. **57**, 1252–1260 (2020).
[27]L. Zeng, G. Liu, D. Yang, and X. Ji, "Cost-efficient laser-diode-induced optical-resolution photoacoustic microscopy for two-dimensional/three-dimensional biomedical imaging," J. Biomed. Opt. **19**, 076017 (2014).
[28]P. K. Upputuri and M. Pramanik, "Dynamic *in vivo* imaging of small animal brain using pulsed laser diode-based photoacoustic tomography system," J. Biomed. Opt. **22**, 1 (2017).
[29]P. K. Upputuri and M. Pramanik, "Performance characterization of low-cost, high-speed, portable pulsed laser diode photoacoustic tomography (PLD-PAT) system," Biomed. Opt. Express **6**, 4118–4129 (2015).
[30]M. A. Richards, J. Scheer, W. A. Holm, and W. L. Melvin, *Principles of Modern Radar* (Citeseer, 2010).
[31]N. Levanon, I. Cohen, N. Arbel, and A. Zadok, "Non-coherent pulse compression—Aperiodic and periodic waveforms," IET Radar Sonar Navig. **10**, 216 (2016).
[32]M. Golay, "Complementary series," IEEE Trans. Inf. Theory **7**, 82 (1961).
[33]N. Levanon, "Noncoherent radar pulse compression based on complementary sequences," IEEE Trans. Aerosp. Electron. Syst. **45**, 742 (2009); available at http://www.eng.tau.ac.il/~nadav/pdf-files/ncpc_complementary.pdf.
[34]M. Xu and L. V. Wang, "Pulsed-microwave-induced thermoacoustic tomography: Filtered backprojection in a circular measurement configuration," Med. Phys. **2**, 1661 (2002).
[35]Y. Xie, B. Guo, J. Li, G. Ku, and L. Wang, "Adaptive and robust methods of reconstruction," IEEE Trans. Biomed. Eng. **55**, 2741 (2008).
[36]G. P. Chen, W. B. Yu, Z. Q. Zhao, Z. P. Nie, and Q. H. Liu, "The prototype of microwave-induced thermo-acoustic tomography imaging by time reversal mirror," J. Electromagn. Waves Appl. **22**, 1565–1574 (2008).
[37]X. Wang, D. R. Bauer, R. Witte, and H. Xin, "Microwave-induced thermoacoustic imaging model for potential breast cancer detection," IEEE Trans. Biomed. Eng. **59**, 2782–2791 (2012).
[38]H. Ammari, J. Garnier, W. Jing, and L. Nguyen, "Quantitative thermo-acoustic imaging: An exact reconstruction formula," J. Differ. Equ. **254**, 1375–1395 (2013).
[39]Y. Hristorva, P. Kuchment, and L. Nguyen, "On reconstruction and time reversal in thermoacoustic tomography in acoustically homogeneous and inhomogeneous media," Inverse Probl. **24**, 055006 (2008).
[40]P. Stefanov and G. Uhlmann, "Thermoacoustic tomography with variable sound speed," Inverse Probl. **25**, 075011 (2009).
[41]J. Qian, P. Stefanov, G. Uhlmann, and H. Zhao, "An efficient Neumann series-based algorithm for thermoacoustic and photoacoustic tomography with variable sound speed," SIAM J. Imaging Sci. **4**, 850 (2011).
[42]B. Treeby and B. Cox, "K-wave: Matlab toolbox for the simulation and reconstruction of photoacoustic wave-fields," J. Biomed. Opt. **15**, 021314 (2010).
[43]B. T. Cox and B. E. Treeby, "Artifact trapping during time reversal photoacoustic imaging for acoustically heterogeneous media," IEEE Trans. Med. Imaging **29**, 387 (2010).
[44]B. E. Treeby, "Acoustic attenuation compensation in photoacoustic tomography using time-variant filtering," J. Biomed. Opt. **18**, 036008 (2013).
[45]J. L. B. Robertson, B. T. Cox, J. Jaros, and B. E. Treeby, "Accurate simulation of transcranial ultrasound propagation for ultrasonic neuromodulation and stimulation," J. Acoust. Soc. Am. **141**, 1726–1738 (2017).
[46]R. Jacobs, M. Alzuhiri, M. Golkowski, and Y. Deng, "Low-power microwave induced thermoacoustic imaging: Experimental study and hybrid FEM modeling," PIER **91**, 265 (2018); available at https://www.jpier.org/PIERC/pierc91/20.18100101.pdf.